JOURNAL OF MATERIALS RESEARCH AND TECHNOLOGY 2023;26:5716–5730

Available online at www.sciencedirect.com

jmr&t Journal of Materials Research and Technology

journal homepage: www.elsevier.com/locate/jmrt

Fatigue life assessment and fracture mechanisms of additively manufactured metal-fiber reinforced thermoplastic hybrid structures produced via ultrasonic joining

Willian S. de Carvalho [a,*], Jonathan Draper [b], Talina Terrazas-Monje [a], Athanasios Toumpis [b], Alexander Galloway [b], Sergio T. Amancio-Filho [a,**]

[a] Graz University of Technology – TU Graz, Institute of Materials Science, Joining and Forming, BMK Endowed Professorship for Aviation, Kopernikusgasse 24/1, 8010 Graz – Austria

[b] University of Strathclyde – UoS, Department of Mechanical & Aerospace Engineering, James Weir Building, 75 Montrose Street, G1 1XJ Glasgow – United Kingdom

ARTICLE INFO

Article history:
Received 8 June 2023
Accepted 30 August 2023
Available online 2 September 2023

Keywords:
Fused filament fabrication
Laser powder bed fusion
Fatigue
Fracture mechanisms
Ultrasonic joining
Hybrid structures

ABSTRACT

Ultrasonic Joining (U-Joining) produces through-the-thickness reinforced (TTR) hybrid joints between thermoplastics and surface-structured metals. The joining parameters were previously optimized to join additively manufactured (AM) 316L stainless steel (316L SS) and 20% short-carbon-fiber-reinforced poly-ether-ether-ketone (PEEK-20CF) to maximize the joints' performance under quasi-static lap shear testing. However, further investigations on the joint's fracture mechanisms and cyclic loading performance are still lacking. Therefore, this study describes the stress distributions, assesses the fracture mechanisms and evaluates the fatigue life of AM 316L SS/PEEK-20CF hybrid joints. A finite element model was developed to clarify the joints' mechanical behavior, and their fatigue performance was assessed under cyclic tensile condition. The fatigue tests were performed at different percentages of the reached ultimate lap shear force (ULSF) and analyzed via two-parameter Weibull distribution and load-life curves for different reliability levels. The results showed that a fatigue life of 1×10^6 cycles could be reached when a load of 1.52 kN, or 42% of the ULSF, is applied, demonstrating the joints' high mechanical performance and potential for engineering applications. Joints reaching the one million cycles threshold were stopped at this mark and tested under quasi-static lap shear to assess their residual force. The results significantly decreased from 3.6 ± 0.3 kN to 2.4 ± 0.5 kN for ULSF and residual force, respectively. Fractography analyses identified polymer delamination, partial TTR pull-out, and interfacial/net-tension failure as the main fracture mechanisms. Polymer detachment in fatigue specimens indicated the influence of secondary bending at low load levels, explaining the reduced residual force.

* Corresponding author.
** Corresponding author.
E-mail addresses: willian.salesdecarvalho@student.tugraz.at (W.S. de Carvalho), sergio.amancio@tugraz.at (S.T. Amancio-Filho).

https://doi.org/10.1016/j.jmrt.2023.08.305

1. Introduction

There is an increasing engineering interest in developing novel processes to integrate carbon-fiber reinforced polymers (CFRP) and metallic alloys into lightweight hybrid structures to increase energy efficiency in transportation applications. Although there are a few well-developed, robust and established joining techniques, they rarely exploit the full lightweight design potential of metal-CFRP hybrid structures [1,2]. The narrow range of CFRPs and metals that fulfill the necessary engineering requirements and their physical and chemical dissimilarities between these materials, limit the number of joining techniques that can be used to produce strong metal-CFRP structures [2,3]. The most used processes for producing metal-CFRP structures are adhesive bonding and mechanical fastening. However, both methods have their own limitations that need to be addressed individually. Adhesive bonding demands surface preparation and special fixtures to keep the parts together during the long adhesive curing process [4,5]. Additionally, adhesive joints are prone to brittle failure and have limited load transferability due to their low out-of-plane strength [6,7]. On the other hand, mechanical fastening involves inserting third parties such as rivets, screws or bolts, which requires through-hole pre-drilling, resulting in increased stress concentration in the area. This method can also potentially cause problems such as corrosion and fatigue cracking [2,8].

Advanced thermo-mechanical processes have been developed to overcome these limitations. Different heating sources can be used in this group of techniques to soften or melt the amorphous and semi-crystalline polymers, respectively, at the metal-CFRP interface either directly or indirectly, allowing the softened or molten material to wet the metal surface, fill its microcavities and form adhesive bonds [2]. Examples of thermo-mechanical joining processes include resistance spot welding [5,9], laser joining [10–12], friction spot joining [13–15], friction stacking joining [16], friction stir welding [17], friction riveting [18,19] and ultrasonic welding or joining [1,20–22] processes. Such techniques generally present several advantages, such as low energy input, localized heat development, automation capability, fast joining cycle, etc. [2,23]. However, these techniques are extremely dependent on the surface condition of the parts, joint geometry, applied joining parameters and environment conditions [24]. Additionally, these processes are applied mostly to flat and thin plates, which hinders their application capability and mechanical performance due to low out-of-plane strength [20,21].

Direct assembly (DA) joining techniques represent a further development of thermo-mechanical techniques, where the surface structuring of the metallic surface takes place prior to the joint formation [25]. As demonstrated in the literature, several manufacturing routes can be used for the surface structuring step, including additive [20,26,27], subtractive [28] or formative processes [29]. The resulting structures are known as through-the-thickness reinforcements (TTRs) and are intended to be introduced into the polymeric material to strengthen the joint [30–33]. Afterward, the hybrid joints are produced by laminating a thermoset or thermoplastic-based composite onto the structured surface, resulting in a joint with enhanced out-of-plane strength and improved loading capabilities. Despite these advantages, DA processes are still in the developmental stages, and only a few thermo-mechanical processes have been used to join the components.

Ultrasonic Joining (U-Joining) was developed in this context as a DA friction-based joining approach capable of jcombining surface-structured metallic components with unreinforced or fiber-reinforced thermoplastics using ultrasonic mechanical vibration [20,34]. Previous studies have addressed the combination of different materials, such as metal-injection-molded (MIM) Ti-6Al-4V and laminated glass-fiber reinforced polyetherimide (GF-PEI) [35], as well as additively manufactured (AM) 316L stainless steel (316L SS) and unreinforced and 20%-carbon-fiber reinforced poly-ether-ether-ketone (PEEK-20CF) [20,21,36]. All these studies indicated that the ultrasonic frictional heating triggered several bonding mechanisms, including micro- and macromechanical interlocking, and adhesion forces, resulting in strong joints with enhanced mechanical capabilities [20]. However, a detailed description of the stress distribution, fracture mechanisms and fatigue performance of the produced U-Joints is available exclusively for MIM Ti-6Al-4V/laminated GF-PEI joints [37] and has not been reported for other materials nor AM hybrid joints. By combining AM and U-Joining techniques, metal-CFRP hybrid components with complex optimized designs can be produced, resulting in a novel manufacturing route for lighter and stronger structures [21,36]. Therefore, the present study aims to develop a finite element model to support the understanding of the U-Joints' stress distribution, investigate the fracture mechanisms and asses the fatigue life of AM 316L SS/PEEK-20CF U-Joints. Both selected materials are interesting for aerospace applications as they are qualified for primary and secondary aircraft structures – e.g. 316L brackets produced via LPBF [38] and laminated CF-PEEK skin panels [38]. The fatigue results were statistically analyzed via two-parameter Weibull distribution and the influence of different reliability levels was explored. Finally, the failure mechanisms were thoroughly investigated to provide a fundamental understanding of the joint failure and fracture mechanisms under different loading conditions.

1.1. *U-joining*

The U-Joining process involves three steps, as shown in Fig. 1. The procedure begins with positioning the parts between the anvil and the sonotrode, where the tool is built, with the structures on the metal surface facing the upper side of the composite, as presented in Step 1. In Step 2, the sonotrode begins to vibrate and apply pressure to the connecting pieces. High-frequency mechanical vibration is converted into heat by two mechanisms in this step: (i) friction between metal and CFRP surfaces, initially between TTR tips and the polymer surface and, once the TTRs are fully inserted, between the metallic and polymer flat surfaces; and (ii) intermolecular friction that results in viscous dissipation [39]. As a result, the polymeric matrix around the metal-CFRP interface softens or melts, allowing the TTRs to be inserted into the composite structure. In Step 3, the vibration stops when the TTRs are fully inserted, and pressure remains constant until the soften or molten layer solidifies. This process accounts for differences in

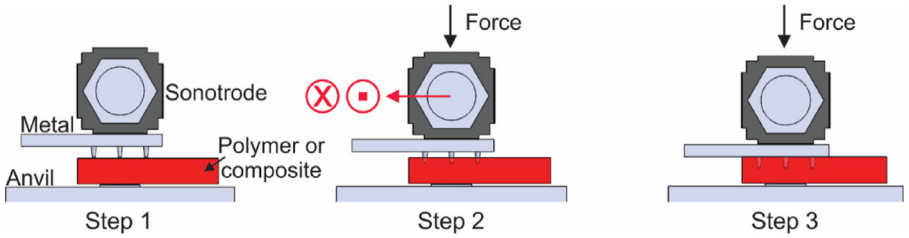

Fig. 1 – U-Joining process steps. Reprinted with authorization from [20].

Table 1 – Chemical composition of the L-PBF 316L SS connectors. Reproduced with authorization from [21].

C	Si	Mn	Cr	Ni	Mo	S	N	V	W	Cu	Fe
0.03	0.76	0.73	17.97	13.67	2.29	0.01	0.05	0.04	0.01	0.04	Bal.

shrinkage rates between the two materials, which could lead to defects at the metal-polymer interface. The joining cycle concludes with the retraction of the sonotrode [20,35].

The combination of mechanical interlocking (due to the contribution of TTRs) and adhesion forces enhances the joint's out-of-plane strength [20,34,35]. Furthermore, complex TTR structures can be produced by adopting the proper structuring method, such as AM, and their density and distribution tailored to the application requirements [30,31,40].

2. Materials and methods

2.1. *Base materials, additive manufacturing techniques and U-Joining setup*

For this investigation, 15.5 x 35 × 3 mm surface-structured connectors made of 316L SS were applied. The connectors presented conical TTRs and were produced through laser powder bed fusion (L-PBF). Carpenter Additive (USA) supplied the pre-alloyed and gas-atomized spherical powder while the printing process was done using a Creator RA machine (Coherent, Germany), with the parts printed with a building angle of 45°. The main L-PBF parameters were pre-optimized [41] and are applied in this study: laser power of 120 W, layer height of 25 μm, printing speed of 1000 mm/s and laser spot diameter of 40 μm. The density of the printed components was measured according to ASTM B962-15 [42] using Archimedes' principle, resulting in a density of 7.8 ± 0.05 g/cm^3 or 98 ± 0.6% compared to bulk material (8 g/cm^3 [43]). The chemical composition of the printed parts was assessed using optical emission spectroscopy (OES) with a Spectrolab M8 (SPECTRO Analytical Instrument, Germany) spectrometer. The obtained values are consistent with the normal nominal values for this alloy [43] and the mean values are presented in Table 1. Fig. 2-a) shows the connectors dimensions and a detailed view of the geometry of the TTRs employed in the study, which was based on earlier research [34,36]. Fig. 2-a) also illustrates an undercut with a radius of 0.2 mm at the base of the TTRs, which was applied to move the stress concentration away from this region and further increase the mechanical interlocking between the materials [35].

Fig. 2-a) also shows the dimensions (15.5 x 35 × 6.35 mm) of the flat fused filament fabricated (FFF) PEEK-20CF samples. The samples were produced using a 1.75-mm-diameter filament supplied by 3DXTech (USA) and printed in a FUNMAT HT (Intamsys, China) FFF 3D-printer. The PEEK-20CF pieces were printed using the previously optimized parameters: building

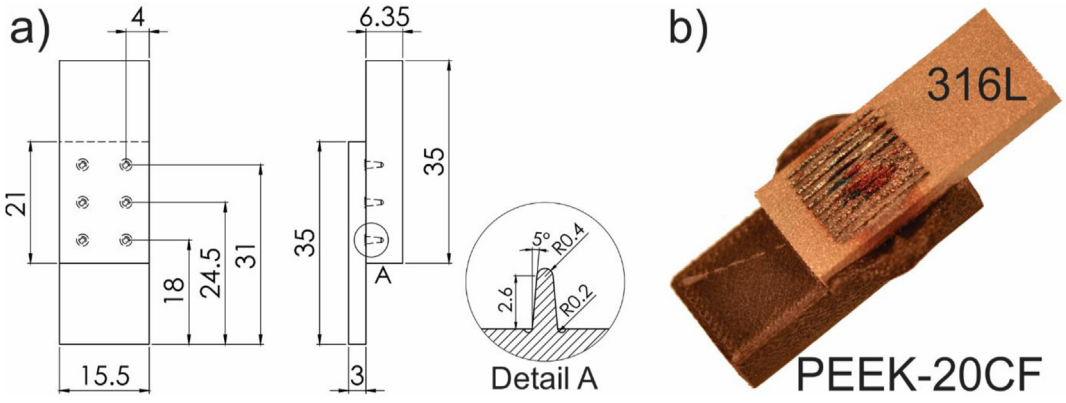

Fig. 2 – a) Dimensions of the overlapped joint and TTRs used, and b) an overview of a produced U-Joint - reprinted with authorization from [21]. All dimensions are given in mm.

chamber temperature of 90 °C, building plate temperature of 160 °C, printing temperature of 385 °C, layer height of 0.1 mm and printing speed of 17.5 mm/s. Before each printing cycle, the building plate surface was coated with polyvinylpyrrolidone (PVP) adhesive to improve part adherence to the platform.

The Ultraweld L20 (Branson Ultrasonics, USA) metal ultrasonic welding system was used for the U-Joining method, which operates with a fixed sonotrode vibration frequency of 20 kHz. Lap shear specimens were joined using the so-called energy mode, which keeps the sonotrode vibration constant until the pre-set energy value is reached. As already described in the literature, an exponential sonotrode was used with a replaceable H13 steel tool [21]. The joints were manufactured with previously optimized U-Joining parameters: joining energy (E_J) of 5000 J, sonotrode amplitude (A_O) of 120 μm and joining pressure (J_P) of 60 psi (approximately 4 bar). J_P is the cylinder pressure along the joining process in this study and its magnitude will be presented in pounds per square inch (psi) for a convention. Fig. 2-b) depicts an overview of a produced U-Joint.

2.2. *Stress distribution analysis via numerical simulation*

To provide a better understanding of the stress distribution in AM 316L SS/PEEK-20CF U-Joints during quasi-static lap-shear loading, a simple finite element (FE) model was developed. From the simulation results, a quantitative discussion would only be possible if property values for the AM materials and the metal-CFRP interface would be determined experimentally and implemented into the model, which falls out of the scope of the present study. In this sense, for the model setup, properties reported in the literature were used and thus, the obtained outcomes served solely for qualitative purposes.

The FE model was developed in Abaqus Standard 2018 (Dassault Systemes, France), considering two solid parts, namely, representing the joint's metal (Fig. 3-a) and fiber-reinforced thermoplastic (Fig. 3-b). Both parts were constructed according to the dimensions presented in Fig. 2. For the metallic part, material properties were obtained from a L-PBF 316L stainless steel material printed at 45° with respect to the printing plate [44], and for the fiber-reinforced thermoplastic part from a short carbon fiber reinforced PEEK composite with a fiber content of 15 wt% [45]. These properties are presented in Table 2 and were considered to be isotropic for all directions.

A plane of symmetry was used along the longitudinal axis of the joint, and the undercut at the TTRs' base was removed to simplify the geometry. Both simplifications reduce the complexity of the model, thus reducing the computational time and the memory required. In addition, encastre and displacement boundary conditions were applied to represent the lap shear test conditions, as indicated in Fig. 3-c). The encastre was applied on the extremity of the metal to represent the stationary clamp of a tensile machine. A displacement of 3 mm, on the other hand, was applied on the opposite end of the polymer and represented the action of a pulling clamp during a displacement-controlled loading process.

To model the adhesion between both parts resulting from the joining process, surface-based cohesive behavior was defined at their interface according to the cohesive-zone-model (CZM), as indicated in Fig. 3-d). The contact pair was defined, with the metal and the fiber-reinforced thermoplastic being the master and slave surfaces, respectively. The cohesive behavior was defined by means of bilinear traction-separation curves for each of the loading modes, assuming a linear elastic behavior, followed by damage initiation and linear damage evolution at the interface. For the cohesive contact formulation, literature-based traction-separation properties were used [46]. Taking

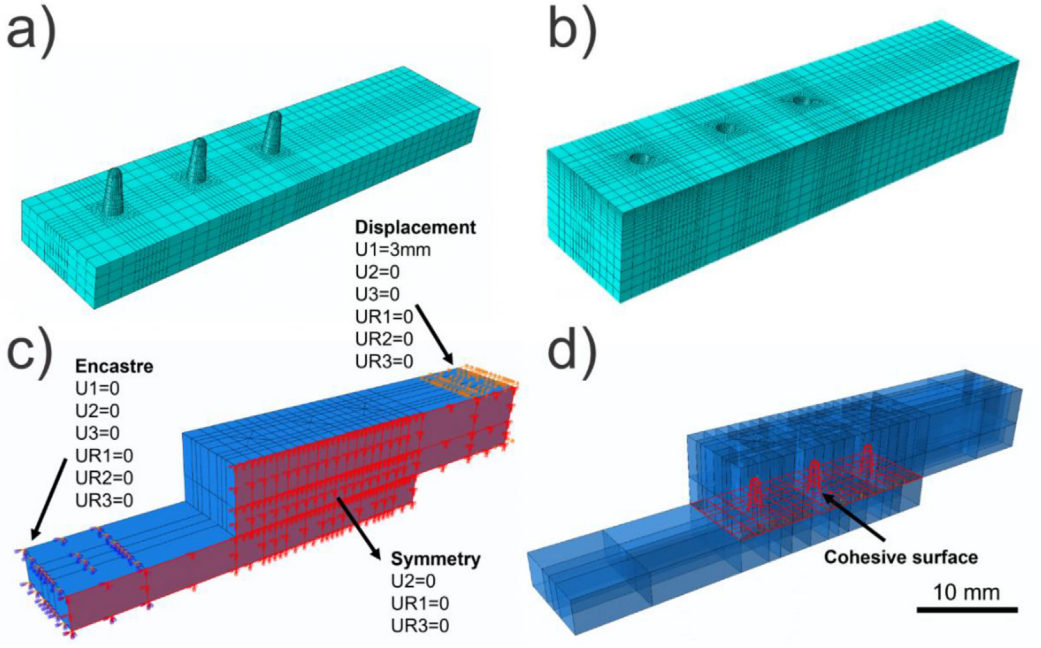

Fig. 3 – a) Metal and b) CFRP parts, c) assembled hybrid-joint for lap shear test and the applied boundary conditions; and d) the cohesive contact surface at the metal-CFRP interface.

Table 2 – Base material properties used in the FE model.

Base material	Young's modulus [MPa]	Yield strength [MPa]
316L SS [44]	197500	539.96
PEEK-15CF [45]	4062	28.28

into account that the debonding under loading modes II and III are both fracture modes caused under transverse shear stress, they were considered to be equal. These values are presented in Table 3. Furthermore, a friction coefficient of 0.37 was obtained from the literature [47] and applied to the metal-CFRP interface.

Finally, for the most part of the assembly, the meshes applied were generated from hexahedral-shaped elements of the type C3D8R (general-purpose 8-node linear brick elements with reduced integration). This element type was chosen because it provides good accuracy at a minimum computational cost in three-dimensional problems. Moreover, in the polymer part, the surroundings of the holes that host the TTRs were meshed with C3D8 elements (general-purpose 8-node linear brick elements fully integrated), due to the higher mesh distortions in these areas. The seeding for the meshes was defined in accordance to the degree of deformation that was expected locally in the model geometry.

2.3. *Quasi-static and cyclic fatigue mechanical tests and fractography analyses*

As mentioned in Section 2.1, the U-Joints used in this study were produced with previously optimized parameters, where the U-Joining parameters were optimized to maximize the ultimate lap shear force (ULSF) reached by the joints. A universal testing machine (Zwick/Roell Group, Germany), equipped with a 100 kN load cell, was used to perform the quasi-static single lap-shear tests at room temperature. These tests were conducted with a crosshead speed of 1 mm/min, and the gripping system was positioned individually to account for the overlap geometry and keep the center line of the joint aligned to the main axis of the testing machine. The ULSF reached by the optimized condition was 3.6 ± 0.3 kN (approximately 11 MPa), and the fractured specimens were analyzed to validate the results obtained by the numerical model and support the understanding of the involved fracture mechanisms. The fractography analysis was conducted via scanning electron microscopy (SEM) using a Tescan Mira 3 (TESCAN, Czech Republic). The joints were carbon sputtered prior to analysis, and the fractured surface was examined using a secondary electron detector with an acceleration voltage of 10 kV, a working distance of 50 mm and a chamber pressure of 10^{-1} Pa.

Table 3 – Cohesive contact parameters used for the 316L SS/PEEK-20CF interface [46].

Penalty stiffness [N/m^3]		Maximum nominal stress [MPa]		Fracture energy [J/m^2]	
K_n	K_s, K_t	t_n	t_s, t_t	G_{IC}	G_{IIC}, G_{IIIC}
444×10^9	200×10^9	9	22	550	7790

Fatigue tests were also performed on optimized U-Joints to assess the cyclic behavior of the produced joints. As presented by Staab and Balle [1] and De Carvalho and Amancio-Filho [20], the bonding mechanisms of metal-CFRP hybrid joints are composed of macro- and micromechanical interlocking, as well as adhesion bonds by softening or melting, and resolidifying the thermoplastic matrix. Additionally, the high quantity of voids and layers inside the PEEK-20CF parts deriving from the FFF process increases the complexity of the failure mechanisms, and influences crack propagation [48]. All these characteristics result in a highly heterogeneous distribution of the local strength of the investigated hybrid structures, making it unsuitable to use strength as a measure for specifying load horizons in cyclic fatigue tests as engineering stress [22]. Therefore, the testing load will be used in the present paper instead of the stress for the fatigue discussions, and L-N curves will be used instead of S-N.

The tests were performed at room temperature using a servo-hydraulic Instron 8801 fatigue testing system (Instron, USA). The geometry of the quasi-static single lap joints (presented in Fig. 2) was used, and specimens were aligned in the gripping system with the help of end tabs. Pure cyclic tension load was applied using a sine-wave loading form with a load ratio (F_{min}/F_{max}) of $R = 0.1$ and at a constant frequency of 5 Hz, as it is often used for aircraft component testing [49]. Four loading conditions were explored in this study, representing percentages of the ULSF reached by the optimized condition (3.6 ± 0.3 kN): 65%, 55%, 45% and 35%. Table 4 displays the conditions of the tests, such as the different loading level percentages and their corresponding loads, as well as the number of cycles until fracture. The stopping criterion considered was the complete failure of the specimen or 1×10^6 cycles. For each level, three replicates were tested to ensure repeatability.

The probability aspects of the fatigue results were analyzed via two-parameter Weibull distribution. Khelif et al. [50] demonstrated that this distribution is preferred over other statistical distributions as it generates more conservative curves and is suitable for complex systems where linear fits are inadequate. Additionally, this distribution also models extreme values such as failure times and limits [51,52]. The probability density function (PDF) for a two-parameter Weibull distribution is defined by Eq. (1):

Table 4 – Load levels and results of fatigue tests for the optimized condition.

Load [%]	F_{max} [kN]	F_{min} [kN]	F_{med} [kN]	F_a [kN]	Cycles [N_f]
65	2.340	0.234	1.287	1.053	41
					129
					290
55	1.980	0.198	1.089	0.891	9365
					11039
					17885
45	1.620	0.162	0.891	0.729	103776
					168344
					164956
35	1.260	0.126	0.693	0.567	>1,000,000
					>1,000,000
					>1,000,000

$$f(x)=\frac{\beta}{\alpha}\left(\frac{x}{\alpha}\right)^{\beta-1}e^{-\left(\frac{x}{\alpha}\right)^{\beta}}\ \alpha\gg 0,\beta\gg 0 \tag{1}$$

Where α and β are the scale (or characteristic life) and shape (i.e. Weibull exponent or slope) parameters, respectively. x represents the number of cycles (N_f) [53,54]. Integrating the PDF equation results in the cumulative density function (CDF). As indicated in Eq. (2), CDF reflects the chance that an element of the population would have a value less than or equal to a given x or N_f.

$$F_f(x)=1-e^{-\left(\frac{x}{\alpha}\right)^{\beta}} \tag{2}$$

The Weibull plot can graphically analyze the fit of a data set to a two-parameter Weibull distribution. These plot features arrange the points linearly if the data follows a Weibull distribution [51]. However, since $F_f(x)$ cannot be obtained by Eq. (2) directly, as it is difficult to test the entire population, the Bernard's Median Rank (MR) empirical estimator (provided by Eq. (3)) was used:

$$MR=\frac{i-0.3}{n+0.4} \tag{3}$$

where i represents the experiment number in ascending order and n is the total number of experiments.

The determination of the Weibull parameters α and β is possible by applying the logarithm function twice in Eq. (1), resulting in Eq. (4):

$$lnln\left[\frac{1}{1-f(x)}\right]=\beta\ lnx-\beta\ ln\ \alpha \tag{4}$$

Plotting the graphs $lnln\left[\frac{1}{1-f(x)}\right]$ versus lnx determines β for each load level, which is equal to the angular coefficient and α since the linear coefficient is equal to $-\beta\ln(\alpha)$.

After calculating the Weibull parameters α and β obtained in the Weibull plot, the Weibull mean life or mean time to failure (MTTF) can be calculated, which reflects the expected life for a given load amplitude for fatigue testing and is represented by Eq. (5):

$$MTTF=\alpha\Gamma\left(1+\frac{1}{\beta}\right) \tag{5}$$

where $\Gamma(\ )$ is the gamma function [53,55].

The coefficient of variation (CV) represented in Eq. (6) is used to assess the relative dispersion across sets of recorded load values, and it represents the ratio of the standard deviation (SD) (Eq. (7)) and the MTTF (Eq. (5)):

$$CV=\frac{SD}{MTTF} \tag{6}$$

where

$$SD=\alpha\sqrt{\Gamma\left(1+\frac{2}{\beta}\right)-\Gamma^2\left(1+\frac{1}{\beta}\right)} \tag{7}$$

Finally, reliability refers to the probability of a component's functional performance under given service conditions over a specific period. The typical reliability levels for aerospace and automotive structural parts range from 80 to 99% [49]. Therefore, in this study, L-N plots were drawn for three different reliability levels: 80, 90 and 99%. These curves provide the possibility of predicting the fatigue life of the joints according to the level of reliability desired by the engineer [51]. Eq. (8) derives from the Weibull distribution, and it will be used to obtain the values of life for different reliability levels:

$$N_{R_x}=\alpha(-\ln(R_x))^{\frac{1}{\beta}} \tag{8}$$

in which N_{RX} is the value of fatigue life of the U-Joints, indicating X% of reliability [51].

After completing the statistical analysis, U-Joints that could withstand one million fatigue cycles without experiencing failure (here called run-out specimens) were tested again under the same quasi-static lap shear conditions as previously specified. The outcomes of these tests have been reported as the residual force of the joints following one million fatigue cycles. Finally, the fractured surface of selected tested fatigue samples was analyzed via SEM using the aforementioned parameters.

3. Results and discussion

3.1. *Stress distribution and fracture mechanisms under quasi-static lap shear testing*

As explained in Section 2.2, the stress distribution in a U-Joint during quasi-static lap shear loading was studied using a FE model. For this purpose, Von Mises stress distributions were evaluated for different time-steps during the simulated loading (see Fig. 4).

Feistauer [56] observed in his work that the loading bearing behavior during quasi-static lap shear testing is heavily influenced by the asymmetric geometry of U-Joints, the presence of TTRs, and the mismatch in material stiffness. In the first instants that the load (F) is applied on the polymer, the bridging effect exerted by the reinforcements already becomes evident, as they start bearing loads almost immediately (Fig. 4-a). The highest stress concentration is seen to occur at the TTRs' bases. As the applied force increases, the metal's yield strength is overcome at the TTRs, and the material starts to plastically deform in the direction of the applied load (Fig. 4-b). An out-of-plane displacement can also be observed between the parts and their respective neutral lines, resulting in an eccentric load path. Overlapping joint configurations often exhibit this phenomenon, creating a resultant moment commonly known as secondary bending (SB) [57,58]. As the test progresses, F and SB induce different local moments (ML) on all the TTRs, presented as M1, M2 and M3 in Fig. 4-c).

Fig. 4 also show that the effects of SB combined with ML can result in an evolution of the failure mechanisms during loading. When the test starts, the three TTRs are subjected to shearing. As the loading continues, however, TTR 3 starts showing a mixture between shearing and pull-out effects. Both mechanisms result in the detachment of the polymer from the metal's surface. TTR 2 presents the same behavior as TTR 3, but with a delayed start of the pull-out. As the crack opening increases, the pull-out contribution to the failure of TTR 3 and TTR 2 increases. Moreover, since a strong SB effect is observed, TTR 3 eventually starts slipping out of the polymeric hole and bearing less shear loads until complete pull-

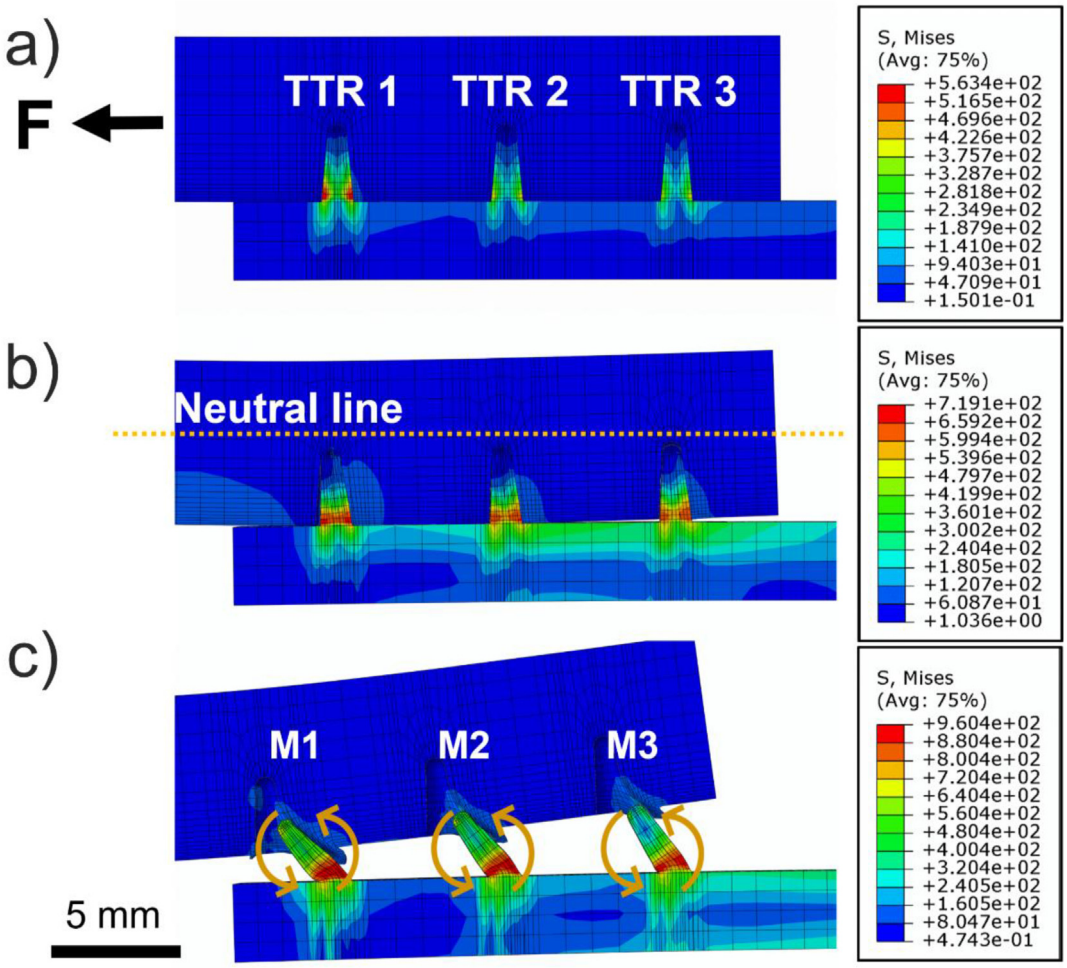

Fig. 4 – Von Mises stress distribution for different step times: a) 0.04 s, b) 0.18 s and c) 1 s.

out is achieved. At even higher displacements, the same behavior is seen for TTR 2 and subsequently for TTR 1.

The discussion above assumes an ideal scenario where both materials can bear the high deformation and stress concentration caused by F, SB and ML until the complete TTR pull-out occurs. In the end, U-Joints behave similarly to multi-fastened joints, where outer fasteners (in this case, the TTRs) bear higher loads and shear stresses than central fasteners [56]. However, as discussed in previous studies, such advanced deformation levels were not yet reported, as the metal [34,35,56] or the polymer [20,21] tend to fail before a complete TTR pull-out. Therefore, by analyzing the U-Joints configuration and the reported fracture mechanisms, four failure modes can take place during a quasi-static lap shear testing of U-Joints: (i) TTR failure, (ii) interfacial failure, (iii) net-tension failure or (iv) TTR pull-out. Fig. 5-a) illustrates the SB moment in a U-Joint; whereas Fig. 5-b) and -c) indicate the different failure modes.

Feistauer [56] analyzed the mechanical performance of MIM Ti-6Al-4V/laminated GF-PEI U-Joints. In his study, he observed a combination of interfacial failure (which can be adhesive, cohesive or a mixture of both), low TTR pull-out and strong TTR failure, as the crack nucleated and propagated

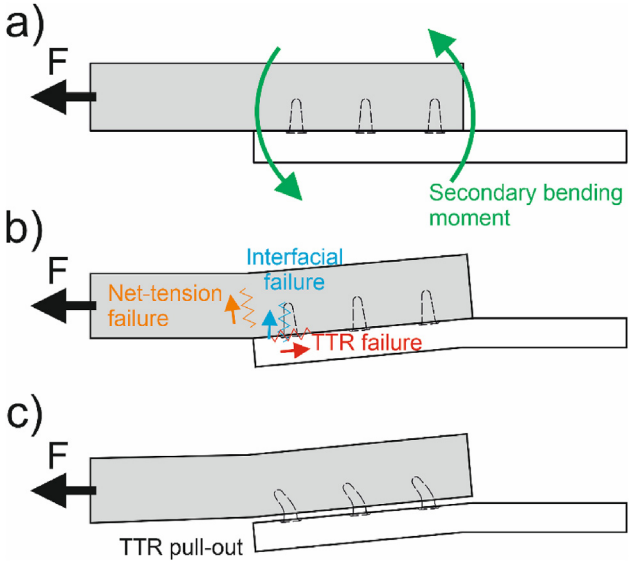

Fig. 5 – a) Representation of a secondary bending moment in a U-Joint; b) and c) show the reported U-Joint fracture modes.

along their base. This behavior is related to the mechanical properties of the metal. As explained in his work, the MIM Ti-6Al-4V presents a low elongation at break of approximately 20%, which resulted in a brittle fracture of the metal, prior to high plastic deformation of the TTRs [56]. On the other hand, in previous studies [20,21], a mixture of interfacial and net-tension failure was observed for AM 316L SS and PEEK-20CF U-Joints, with low pull-out levels at the tips of the used TTRs. Therefore, although the AM 316L presents a high elongation at break of approximately 50% [59], which could result in a ductile joint behavior, a premature joint failure was reported. As a deep investigation to explain this behavior was not conducted in these prior studies, the present manuscript addressed that knowledge gap by conducting a fractography analysis of AM 316L SS/PEEK-20CF U-Joints after a quasi-static lap shear test. The obtained results are presented in Fig. 6.

Fig. 6-a) presents an overview of the fractured U-Joint after quasi-static lap shear testing, which indicates a mix of different failure modes. Firstly, it can be observed that the polymer delaminated completely at a specific position. As Sikder et al. [60] explained, PEEK specimens processed by FFF present weak interlayer adhesion even for optimized FFF parameters, which can result in this type of failure. Fig. 6-a) also indicates partial pull-out of the TTRs, as the tips of the TTRs are exposed, and holes are left on the surface of the composite part. Fig. 6-b) shows an SEM overview of the fractured surface indicated by the arrows in Fig. 6-a). Analyzing the sample from this angle shows that interfacial and net-tension failure modes occurred in this direction, around the first row of TTRs. Fig. 6-c) shows a detailed side view of one exposed TTR, where a considerable PEEK-20CF quantity remained attached to the surface of the metal, with some of the metal exposed. This indicates an interfacial failure by a mixture of adhesive and cohesive modes, demonstrating that the molten polymer had efficiently wetted out the 316L surface, forming strong adhesion forces after joint consolidation. Additionally, the images demonstrate that the rough metallic surface produced by the L-PBF process enhanced the micromechanical interlocking of the materials, therefore improving the joint's mechanical performance.

Additional regions were analyzed and are presented in Fig. 6-d) – f) to describe the net-tension micro failure features of the CFRP. The circular dashed highlighted regions in Fig. 6-d) and e) indicate the presence of a large number of volumetric defects, which can be associated with intra and inter-bead voids and (ii) thermal-induced defects, such as entrapped

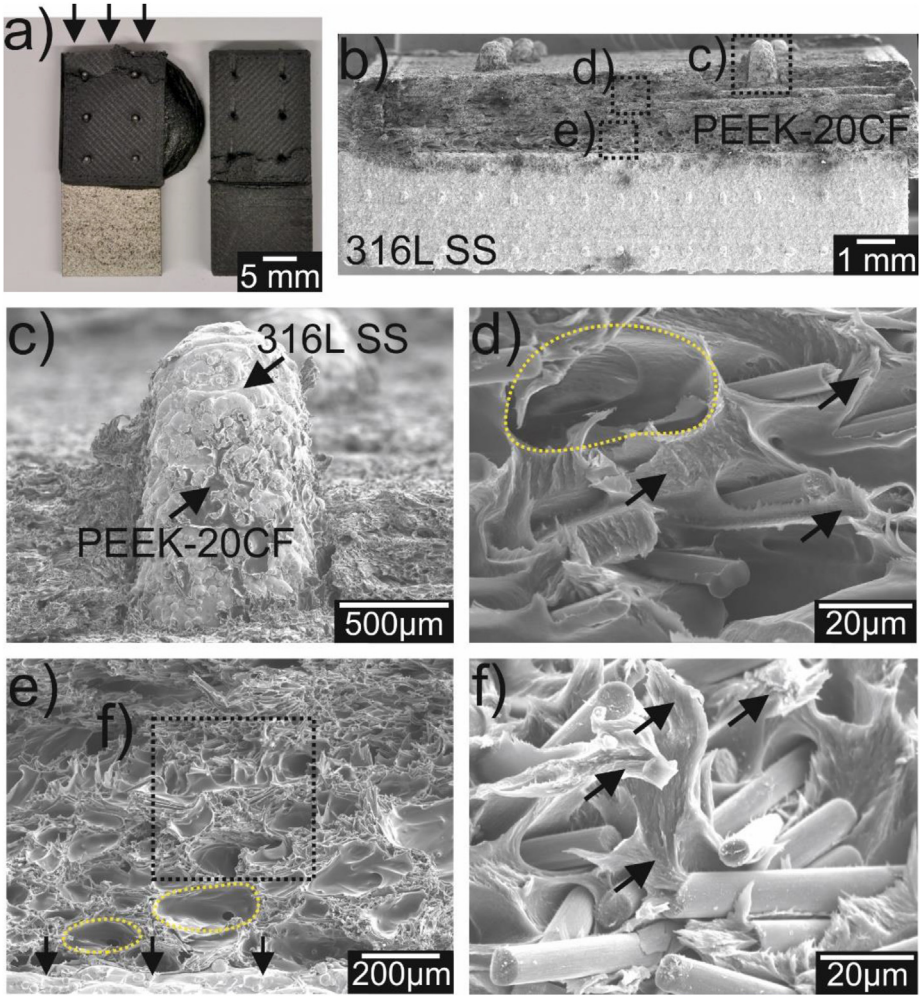

Fig. 6 – a) Fractured U-Joint after quasi-static lap shear test; b) SEM overview of the fractured surface; c) – f) show detailed views of selected regions.

gases during the solidification of the polymer after the joining process – which can be products of thermal decomposition or moisture evolution [61,62]. Fig. 6-d) and -f) also show extensive fiber pull-out with a clear surface (i.e., without polymer residues), indicating a poor adhesion between fibers and matrix. This low impregnation reduces the maximum reinforcement the fibers can bear and their capability to transfer the loads properly to the matrix. Matrix yielding can also be observed and indicated by the arrows in Fig. 6-d) and -f); however, due to the high presence of volumetric defects and carbon fiber content, one can observe that the matrix area is only a fraction of the total area. Fig. 6-e) also indicates that the polymer did not suffer any detachment at the metal-CFRP flat interface (area indicated by the arrows), which could have occurred due to the SB, as indicated by Fig. 4. A mixture of four different failure modes were thus identified in AM 316L SS/PEEK-20CF U-Joints tested under quasi-static lap shear testing: these were polymer delamination, partial TTR pull-out, interfacial and net-tension.

3.2. *Fatigue life assessment and fracture mechanisms under quasi-static and cyclic lap shear testing*

The applied conditions were already presented in Table 4, and by using Eqs. (2)–(4), the Weibull plots for the different load conditions could be obtained and are presented in Fig. 7. Since none of the samples tested for 35% of the maximum load failed, this dataset was not further used in the analysis.

By analyzing the plots in Fig. 7, it is possible to obtain the scale (α) and shape (or slope, β) parameters by linear regression. This last one can be drawn out keeping in mind that the linear coefficient is equal to $-\beta \ln(\alpha)$. The values of α and β for each load condition, as well as the Weibull mean life (MTTF) obtained from Eq. (5) are presented in Table 5.

Based on the obtained values for MTTF, the L-N curve could be plotted and is presented in Fig. 8. A trend curve was additionally calculated based on the displayed power function and is also included. The use of a power function was inspired by different works that proved the prediction capability of this model for joined specimens [51,63]. The high correlation coefficient $R^2 = 0.9571$ obtained by adjusting the curves to the data indicates a good fit for the Weibull data and its reliability in predicting the fatigue life of the samples.

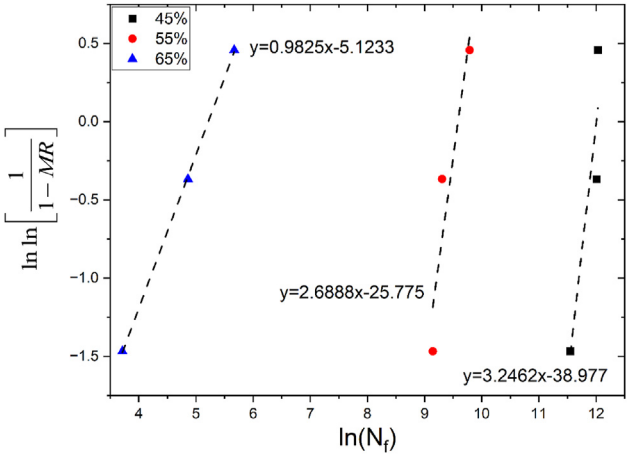

Fig. 7 – Weibull plots for the different load levels tested.

Table 5 – Weibull parameters and mean life for each force amplitude analyzed.

F_{max} [kN]	F_a [kN]	Scale parameter (α) [cycles]	Shape parameter (β)	Weibull mean life [cycles]
2.340	1.053	184	0.9825	185
1.980	0.891	14560	2.6888	12946
1.620	0.729	163892	3.2462	146893

The obtained power function in Fig. 8 predicts that the fatigue life at 1×10^6 cycles is 1.51 kN. This load value represents approximately 42% of the ULSF reached by the specimens under quasi-static test and is close to the only value reported in the literature for U-Joints by Feistauer [56]. In his study, the fatigue performance of MIM Ti-6Al-4V/laminated GF-PEI U-Joints was evaluated and the fatigue life was calculated as 1.68 kN, representing 46% of the achieved ULSF.

Eq. (6) was used to calculate the relative coefficients of variation (CV) for each mean life to assess the consistency of the data. Designers and engineers can use this information for accuracy and repeatability purposes. Fig. 9 illustrates the changes in CV values in relation to the MTTF values at different loading levels.

According to the results in Fig. 9, the higher the used load, the higher the scatter in fatigue life values. The CV reached by the highest load tested (65%) represents the extreme of this condition, where a SD of about 100% of the mean life is reached. This result shows that, at this loading level, the high variability of the analyzed response makes a correct prediction of fatigue performance extremely difficult. By reducing the load, it can be observed that the results become more and more stable, but still do not reach the desired 10%, which is the common threshold to assume that the difference in values indicates no statistical significance [64]. Usually, it is common agreement that CV has to be between 1 and 30% for engineering applications, which are levels reached only by the samples tested with the lowest analyzed condition (45%) [65,66]. Consequently, it can be assumed that the mechanical performance of the analyzed U-Joints becomes more reliable at lower testing loads. As mentioned in previous publications, this behavior is not common in other friction-based joining techniques when materials produced via traditional methods are used, such as rolled sheets [51,67]. However, as discussed in Fig. 6, the used CFRP additively manufactured via FFF process presented a large number of intrinsic volumetric defects and poor fiber-matrix coupling, which can explain the low reliability in the obtained values when high tensile loads are applied.

Fig. 10 shows the L-N curves considering three different reliability levels: 80, 90 and 99%, plotted using Eq. (8). In the case of primary aircraft structural applications, where safety is a significant concern, a high-reliability level is required, such as 90% or 99%, since these guarantee greater chances of joint survival [68]. The reason is that the higher the reliability level, the shorter the fatigue life for a given load, ensuring a greater probability of survival of the joints. This effect is shown by the curves when higher loads are applied.

The obtained L-N curves in Fig. 10 indicate a low variation of the joint performance for low loads, confirming the behavior reported by CV. Furthermore, the fatigue life for all

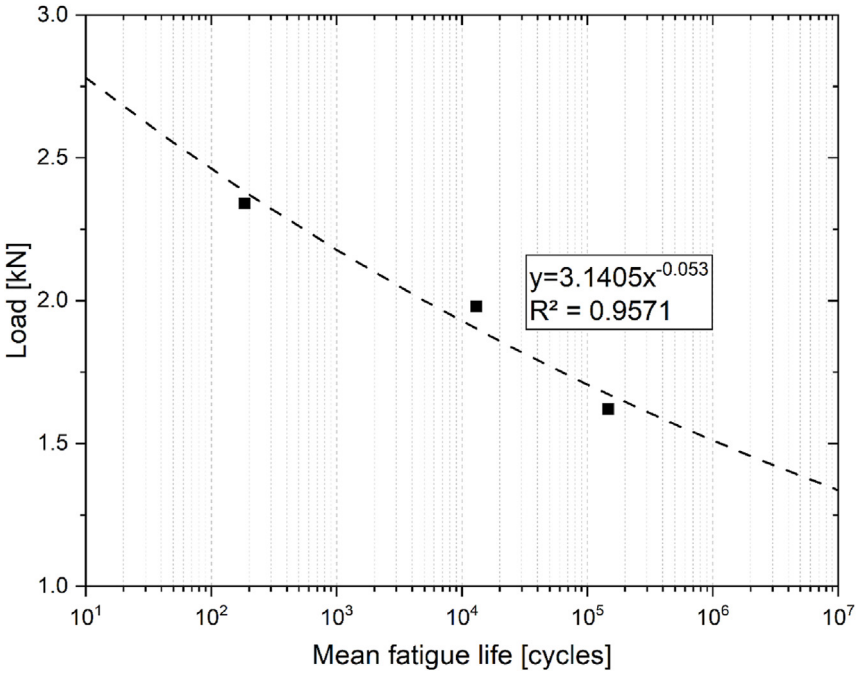

Fig. 8 – L-N curve of AM 316L SS/PEEK-20CF U-Joints.

the analyzed reliability levels at 1×10^6 cycles is approximately 1.52 kN, corresponding to the same 42% of the ULSF achieved by the power function in Fig. 8. Therefore, the fatigue life at 1×10^6 cycles for AM 316L SS/PEEK-20CF U-Joints can be specified at approximately 1.52 kN or approximately 42% of ULSF. The value reached is enough to meet aircraft requirements, which demand a minimum fatigue life for bolted structures between 30 and 35% of their quasi-static strength [69]. Additionally, this value is similar to the 41% (or 1.49 kN) reported for MIM Ti-6Al-4V/laminated GF-PEI U-Joints [56]. However, as different materials produced by different processes were applied, this coincidence cannot be treated as a general behavior of U-Joints and must be further evaluated for different material combinations.

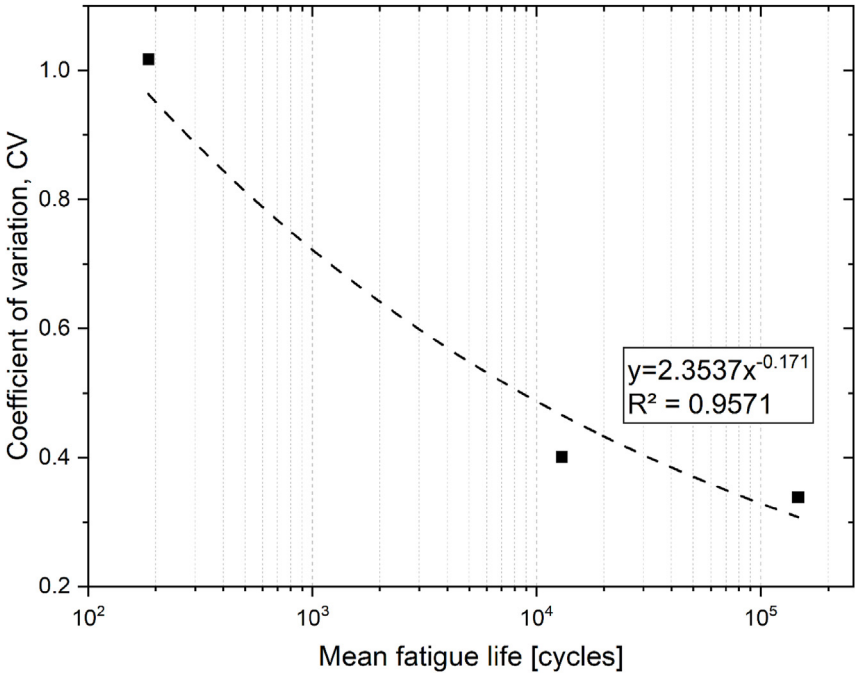

Fig. 9 – Effect of the mean fatigue life on the coefficients of variation.

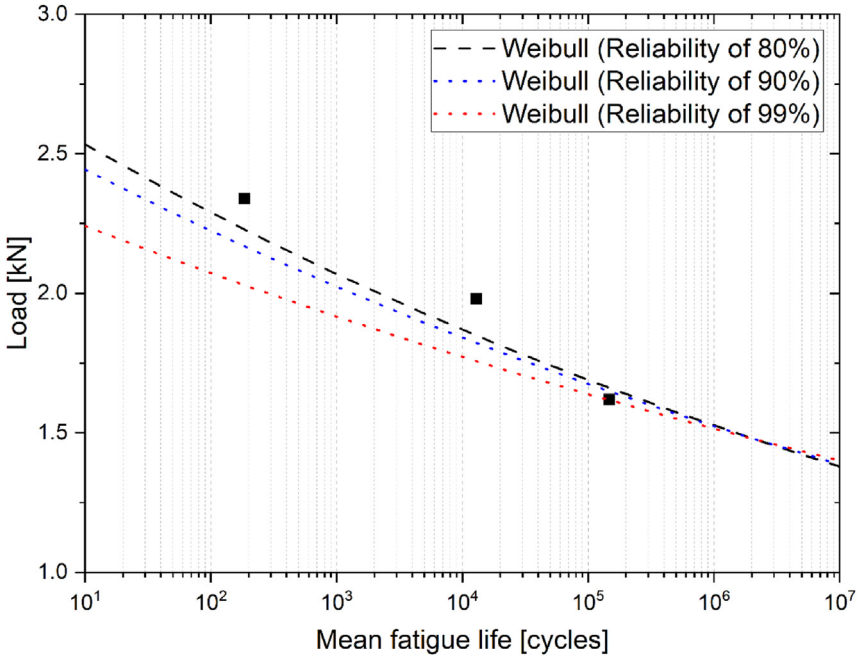

Fig. 10 – L–N curves for different reliability levels.

The present study defined the fatigue limit as 1×10^6 cycles. Consequently, the samples tested at 35% were stopped when they reached this value and since the used value (1.26 kN) was below the 1.52 kN indicated by the power law and Weibull analyses, it is reasonable to assume that the load used would not cause fatigue failure. To verify this hypothesis and validate the identified fatigue life value, these specimens were subsequently tested under quasi-static lap shear testing, using the same procedure outlined in Section 2.3. The achieved ultimate force is called quasi-static lap shear residual force (LSRF) and is compared with ULSF in Fig. 11.

The presented values in Fig. 11-a) show that the LSRF of the fatigued specimens showed a significant reduction when compared to ULSF from 3.6 ± 0.3 kN to 2.4 ± 0.5 kN, or from 11 MPa to 7.4 MPa, respectively. Fig. 11-b) compares two representative curves, demonstrating that this reduction did not influence the curve profile. These results indicate that fatigue damage was introduced and accumulated during the test at the selected level (35% or 1.26 kN). Therefore, it is possible to affirm that such a load level cannot be used as the fatigue endurance limit. To explain this behavior, a fractography analysis was conducted on the residual samples after the lap shear test and the results were compared with Fig. 6. The obtained images for this condition are presented in Fig. 12.

Fig. 12-a) shows that the U-Joint presents the same global fracture behavior as the joints tested directly under quasi-static lap shear (Fig. 6), even after one million fatigue cycles. Fig. 12-b) shows an SEM overview of the fractured surface indicated by the arrows in Fig. 12-a), which demonstrates that interfacial and net-tension failure modes occurred in this direction, around the first row of TTRs. Fig. 12-c) shows a

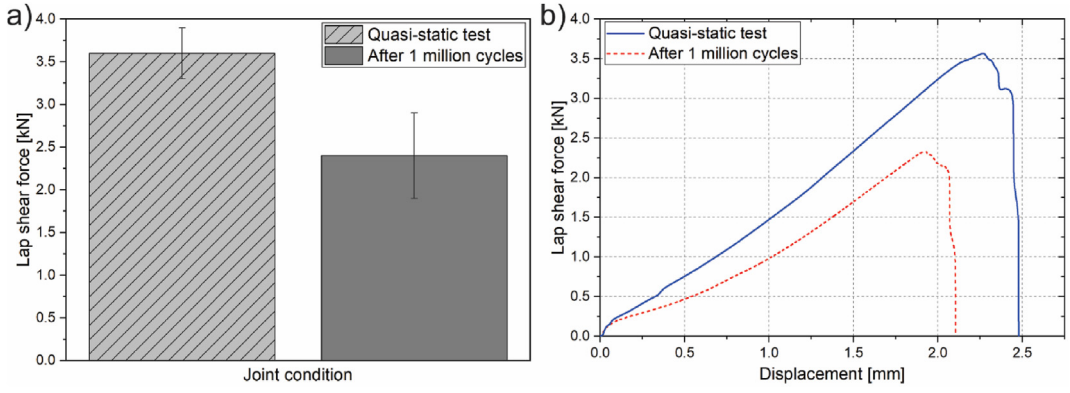

Fig. 11 – a) Comparison between ULSF and LSRF of the joints after one million fatigue cycles, and b) representative curves for both conditions.

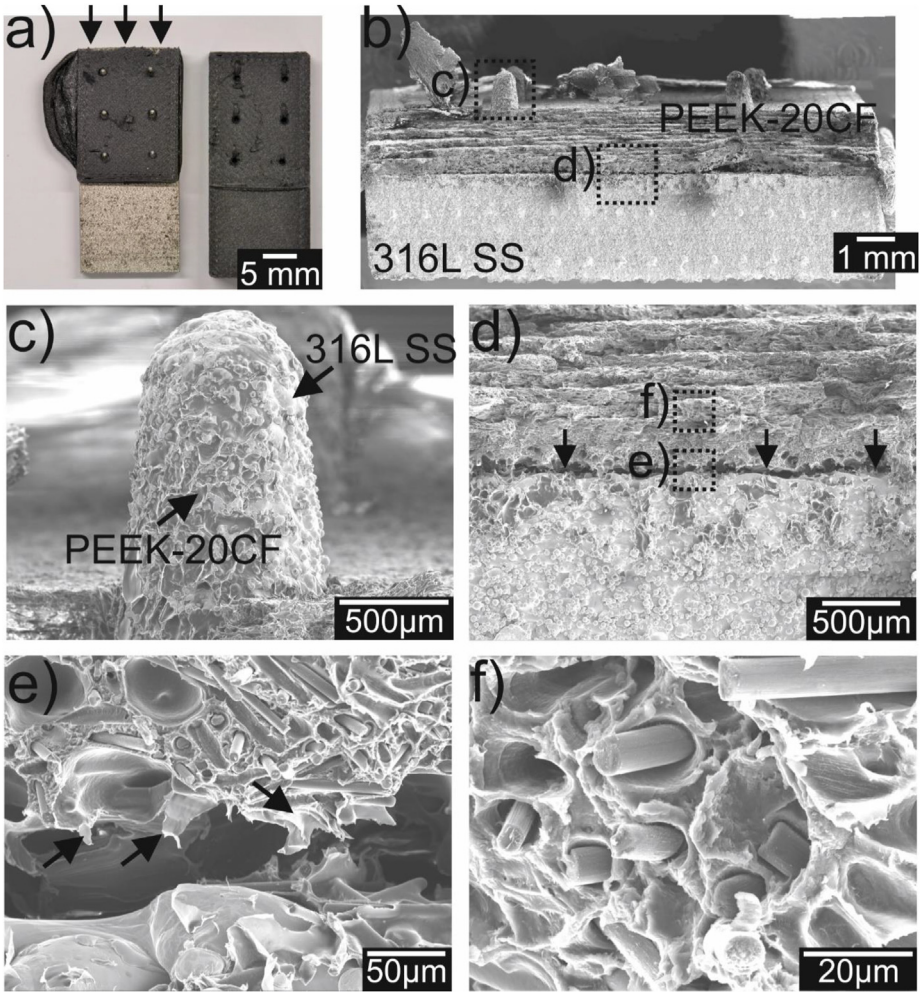

Fig. 12 – a) Fractured U-Joint after 1 million fatigue cycles and subsequent quasi-static lap shear test; b) SEM overview of a fracture surface; c) – f) detailed view of the fracture surface.

considerable PEEK-20CF quantity remained attached to the surface of the metal, with some exposed metal surface. However, the main difference between the samples tested under fatigue and lap shear as also those tested only under lap shear is presented in Fig. 12-d). Here, it is possible to observe that, contrary to Fig. 6, the polymer did detach from the metal surface, as indicated by the arrows. Fig. 12-e) shows a detailed view of the metal-CFRP interface. Here, the presence of fibrils (indicated by the arrows) evidence that, initially, both materials were adhered to each other [25]. As discussed in Fig. 4, the SB effects pulls the polymer from the metal surface, as the crack opening increases, resulting in the polymer dissipating strain energy by undergoing plastic deformation [70]. This effect was not directly observed for quasi-static tests, as the polymer failed before any sign of SB was observed. This detachment may explain the residual force decrease observed after 1 million fatigue cycles described in Fig. 11. The fact that Fig. 12-f) shows the same type of fracture presented in Fig. 6-d) and -f) corroborates that idea, as a change in the involved micro-failure mechanisms was not identified. However, as observed by Zhang et al. [71], extended microcracks nucleation occurs during CFRP fatigue tests. Considering that the FFF process introduces additional defects (such as the previously observed voids), one cannot neglect that the fatigue tests might have introduced microcracks into the polymeric matrix, which could further clarify the reduction in the residual force. Nevertheless, a higher number of microcracks was not observed in the presented SEM images. To conclude, it is possible to affirm that the fatigue tests allowed the visualization of SB-induced effects on U-Joints, and further validated the model presented in Fig. 4.

4. Conclusions

The present work described in detail the stress distributions, the fracture mechanisms and assessed the fatigue life of additively manufactured (AM) 316L stainless steel (316L SS) and 20% short-carbon-fiber reinforced PEEK (PEEK-20CF) hybrid joints produced via ultrasonic joining (U-Joining). The following conclusions can be drawn from the obtained results.

- A finite element (FE) model was developed and demonstrated that, during quasi-static lap-shear tests, the highest

stress concentrations occur at the through-the-thickness reinforcements (TTRs). The model also revealed that the joint's asymmetric geometry, the presence of TTRs, and the material stiffness mismatch could lead to an out-of-plane displacement commonly known as secondary bending (SB).

- U-Joints were tested under quasi-static single lap-shear tests to validate the obtained FE model. Fractography analyses of tested specimens revealed complete delamination of the PEEK-20CF (indicating weak interlayer adhesion within the AM part), interfacial (mixture of adhesive and cohesive), net-tension failure modes, and partial TTR pull-out.
- The fatigue life of the U-Joints was assessed under single-lap shear testing considering different percentages of the joint's ultimate lap shear force (ULSF). The stopping criterion considered was the complete failure of the specimen or 1×10^6 cycles. The results were used to plot an L-N curve based on a power-law model and were statistically analyzed via a two-parameter Weibull distribution for different reliability levels. The results indicate that the fatigue load for 1×10^6 cycles is approximately 1.52 kN, or 42% of the ULSF.
- Joints that endured 1×10^6 fatigue cycles were stopped at this mark and further tested under quasi-static testing. The results show a significant reduction compared to ULSF from 3.6 ± 0.3 kN to 2.4 ± 0.5 kN, indicating that the endurance limit should be at lower values. Additionally, the fractography analyses revealed polymer detachment at the metal-CFRP interface, which can be attributed to the SB effects. This effect was not directly observed for the quasi-static test, as the polymer failed before any sign of SB was identified.

Funding

The authors gratefully acknowledge financial support from the Austrian aviation program "TAKEOFF" (PILOT, grant number 852796, 2018) and BMK – The Austrian Ministry for Climate Action, Environment, Energy, Mobility, Innovation and Technology.

Author contributions/Credit author statement

Conceptualization, W·S.d.C.; methodology, W·S.d.C., J. D., T.T.-M., A.T., A.G. and S.T.A.-F.; formal analysis, W·S.d.C., J.D. and T.T.-M.; investigation, W·S.d.C., J.D. and T.T.-M.; resources, A.T., A.G. and S.T.A.-F.; writing—original draft preparation, W·S.d.C.; writing—review and editing, W·S.d.C., J. D., T.T.-M., A.T., A.G. and S.T.A.-F.; supervision, A.T. and S.T.A.-F. All authors have read and agreed to the published version of the manuscript.

Declaration of competing interest

The authors declare that they have no known competing financial interests or personal relationships that could have appeared to influence the work reported in this paper.

Acknowledgments

The authors would like to acknowledge Branson Ultrasonics for kindly making the Ultraweld L20 joining equipment available. The authors also acknowledge the Open Access Funding by the Graz University of Technology.

REFERENCES

[1] Staab F, Balle F. Fatigue and fracture of ultrasonically welded aluminum alloys to carbon fiber reinforced thermoplastics. Fatig Fract Eng Mater Struct Feb. 2022;45(2):607–16. https://doi.org/10.1111/FFE.13622.

[2] Amancio-Filho ST, Blaga LA. Joining of polymer-metal hybrid structures: principles and applications. Join. Polym. Hybrid Struct. Princ. Appl. Jan. 2018:1–394. https://doi.org/10.1002/9781119429807.

[3] de Carvalho WS, Vioreanu MC, Lutz MRA, Cipriano GP, Amancio-Filho ST. The influence of tool wear on the mechanical performance of aa6061-T6 refill friction stir spot welds. Materials Nov. 2021;14(23):7252. https://doi.org/10.3390/MA14237252. 2021, Vol. 14, *Page* 7252.

[4] Doshi SM, Lyness TB, Thostenson ET. Damage monitoring of adhesively bonded composite-metal hybrid joints using carbon nanotube-based sensing layer Jan. 2020;6(1):12–21. https://doi.org/10.1080/20550324.2019.1699229. doi: 10.1080/20550324.2019.1699229.

[5] Ren S, Ma Y, Saeki S, Iwamoto Y, Ma N. Numerical analysis on coaxial one-side resistance spot welding of Al5052 and CFRP dissimilar materials. Mater Des Mar. 2020;188:108442. https://doi.org/10.1016/J.MATDES.2019.108442.

[6] Bodjona K, Fielding S, Heidari-Rarani M, Lessard L. Effect of adhesive layer compliance on strength of single-lap hybrid bonded-bolted joints. Compos Struct Apr. 2021;261:113324. https://doi.org/10.1016/J.COMPSTRUCT.2020.113324.

[7] Jongbloed BCP, Teuwen JJE, Benedictus R, Villegas IF. A study on through-the-thickness heating in continuous ultrasonic welding of thermoplastic composites. Materials Nov. 2021;14(21):6620. https://doi.org/10.3390/MA14216620. 2021, Vol. 14, *Page* 6620.

[8] Messler RW. Joining of materials and structures: from pragmatic process to enabling technology. Join. Mater. Struct. From Pragmatic Process to Enabling Technol. 2004:1–790. https://doi.org/10.1016/B978-0-7506-7757-8.X5000-3.

[9] Zhang Y, Shan H, Li Y, Guo J, Luo Z, Ma CY. Joining aluminum alloy 5052 sheets via novel hybrid resistance spot clinching process. Mater Des Mar. 2017;118:36–43. https://doi.org/10.1016/J.MATDES.2017.01.017.

[10] Zhang Z, Shan J, Tan X. Evaluation of the CFRP grafting and its influence on the laser joining CFRP to aluminum alloy Feb. 2017;32(4):390–406. https://doi.org/10.1080/01694243.2017.1357457.

[11] Schricker K, Samfaß L, Grätzel M, Ecke G, Bergmann JP. Bonding mechanisms in laser-assisted joining of metal-polymer composites. J. Adv. Join. Process. Mar. 2020;1:100008. https://doi.org/10.1016/J.JAJP.2020.100008.

[12] Lambiase F, Genna S. Experimental analysis of laser assisted joining of Al-Mg aluminium alloy with Polyetheretherketone (PEEK). Int J Adhesion Adhes Aug. 2018;84:265–74. https://doi.org/10.1016/J.IJADHADH.2018.04.004.

[13] Esteves JV, Goushegir SM, dos Santos JF, Canto LB, Hage E, Amancio-Filho ST. Friction spot joining of aluminum AA6181-T4 and carbon fiber-reinforced poly(phenylene

sulfide): effects of process parameters on the microstructure and mechanical strength. Mater Des Feb. 2015;66(PB):437–45. https://doi.org/10.1016/J.MATDES.2014.06.070.
[14] André NM, dos Santos JF, Amancio-Filho ST. Evaluation of joint formation and mechanical performance of the aa7075-T6/CFRP spot joints produced by frictional heat. Materials Mar. 2019;12(6):891. https://doi.org/10.3390/MA12060891. 2019, Vol. 12, *Page* 891.
[15] André NM, Goushegir SM, dos Santos JF, Canto LB, Amancio-Filho ST. Influence of the interlayer film thickness on the mechanical performance of AA2024-T3/CF-PPS hybrid joints produced by friction spot joining Jan. 2017;32(1):1–10. https://doi.org/10.1080/09507116. 2017.1347319.
[16] Huang Y, Meng X, Xie Y, Li J, Wan L. New technique of friction-based filling stacking joining for metal and polymer. Composites Part B Apr. 2019;163:217–23. https://doi.org/10.1016/J.COMPOSITESB.2018.11.050.
[17] Huang Y, Meng X, Xie Y, Li J, Wan L. Joining of carbon fiber reinforced thermoplastic and metal via friction stir welding with co-controlling shape and performance. Composer Part A Appl Sci Manuf Sep. 2018;112:328–36. https://doi.org/10.1016/J.COMPOSITESA.2018.06.027.
[18] Meng X, Huang Y, Xie Y, Li J, Guan M, Wan L, et al. Friction self-riveting welding between polymer matrix composites and metals. Composer Part A Appl Sci Manuf Dec 2019;127:105624. https://doi.org/10.1016/J.COMPOSITESA.2019.105624.
[19] Cipriano GP, de Carvalho WS, Vilaça P, Amancio-Filho ST. Thermomechanical modeling of the metallic rivet in friction riveting of amorphous thermoplastics. Weld World May 2021;65(5):855–64. https://doi.org/10.1007/S40194-020-01049-0/FIGURES/7.
[20] de Carvalho WS, Amancio-Filho ST. On the feasibility of joining additively-manufactured 316L stainless steel and poly-ether-ether-ketone by ultrasonic energy. Addit. Manuf. Lett. Dec. 2022;3:100098. https://doi.org/10.1016/J.ADDLET.2022.100098.
[21] De Carvalho WS, Colvin NF, Benatar A, Amancio-Filho ST. Ultrasonic joining of additively manufactured metal-composite hybrid joints: a Comparison between vertical and horizontal vibration modes. Met Feb. 2023;13(2):319. https://doi.org/10.3390/MET13020319. 2023, Vol. 13, *Page* 319.
[22] Staab F, Liesegang M, Balle F. Local shear strength distribution of ultrasonically welded hybrid Aluminium to CFRP joints. Compos Struct Sep. 2020;248:112481. https://doi.org/10.1016/J.COMPSTRUCT.2020.112481.
[23] Lambiase F, Balle F, Blaga LA, Liu F, Amancio-Filho ST. Friction-based processes for hybrid multi-material joining. Compos Struct Jun. 2021;266:113828. https://doi.org/10.1016/J.COMPSTRUCT.2021.113828.
[24] Amancio-Filho ST. Metal-polymer multi-material structures and manufacturing techniques in transportation. Met. Multi-Material Struct. Manuf. Tech. Transp. Jul. 2020;186. https://doi.org/10.3390/BOOKS978-3-03936-151-9.
[25] Feistauer EE, dos Santos JF, Amancio-Filho ST. A review on direct assembly of through-the-thickness reinforced metal–polymer composite hybrid structures. Polym Eng Sci Apr. 2019;59(4):661–74. https://doi.org/10.1002/PEN.25022.
[26] Oluleke R. Metallurgical performance of hyper - joints in composite to metal joining. Ph.D. Diss. Univ. Manchester; 2015. Accessed: Oct. 28, 2022. [Online]. Available: https://www.research.manchester.ac.uk/portal/en/theses/metallurgical-performance-of-hyper–joints-in-composite-to-metal-joining(6a87e957-d6f1-4d78-b989-a68dc39d41cf).html.
[27] Oliveira GHM, Belei C, de Carvalho WS, Canto LB, Amancio-Filho ST. On the fully additive manufacturing of PC/AlSi10Mg hybrid structures. Mater Lett Jan. 2023;330:133378. https://doi.org/10.1016/J.MATLET.2022.133378.
[28] Di Giandomenico V. Surface structured bonded composite-metal joint. Ph.D. Diss. Cranf. Univ.; 2014. Oct. 28, 2022. [Online]. Available: https://dspace.lib.cranfield.ac.uk/handle/1826/9308.
[29] Earl C, Castrejón-Pita JR, Hilton PA, O'Neill W. The dynamics of laser surface modification. J Manuf Process Jan. 2016;21:214–23. https://doi.org/10.1016/J.JMAPRO.2015.10.002.
[30] Ucsnik S, Scheerer M, Zaremba S, Pahr DH. Experimental investigation of a novel hybrid metal–composite joining technology. Composer Part A Appl Sci Manuf Mar. 2010;41(3):369–74. https://doi.org/10.1016/J.COMPOSITESA.2009.11.003.
[31] Parkes PN, Butler R, Meyer J, de Oliveira A. Static strength of metal-composite joints with penetrative reinforcement. Compos Struct Dec. 2014;118(1):250–6. https://doi.org/10.1016/J.COMPSTRUCT.2014.07.019.
[32] Smith F. Comeld™: an innovation in composite to metal joining. Mater Technol 2016;20(2):91–6. https://doi.org/10.1080/10667857.2005.11753117.
[33] Ucsnik SA, Kirov G. New possibility for the connection of metal sheets and fiber reinforced plastics. Mater Sci Forum 2011;690:465–8. https://doi.org/10.4028/WWW.SCIENTIFIC.NET/MSF.690.465.
[34] Feistauer EE, Guimarães RPM, Ebel T, Dos Santos JF, Amancio-Filho ST. Ultrasonic joining: a novel direct-assembly technique for metal-composite hybrid structures. Mater Lett May 2016;170:1–4. https://doi.org/10.1016/J.MATLET.2016.01.137.
[35] Feistauer EE, dos Santos JF, Amancio-Filho ST. An investigation of the ultrasonic joining process parameters effect on the mechanical properties of metal-composite hybrid joints. Weld World Sep. 2020;64(9):1481–95. https://doi.org/10.1007/S40194-020-00927-X/FIGURES/15.
[36] W. S. de Carvalho and S. T. Amancio-Filho, "Ultrasonic joining of additively manufactured metal-polymer lightweight hybrid structures," in Annual Technical Conference - ANTEC, Conference Proceedings, vol. 1, p. 526.
[37] Feistauer EE, Amancio-Filho ST. Ultrasonic joining of lightweight alloy/fiber-reinforced polymer hybrid structures. Join. Polym. Hybrid Struct. Princ. Appl. Jan. 2018:307–33. https://doi.org/10.1002/9781119429807.CH11.
[38] Pradeep PI, Kumar VA, Sriranganath A, Singh SK, Sahu A, et al. Characterization and qualification of LPBF additively manufactured AISI-316l stainless steel brackets for aerospace application. Trans Indian Natl Acad Eng 2020 53 Aug. 2020;5(3):603–16. https://doi.org/10.1007/S41403-020-00159-X.
[39] Villegas IF, Bersee HEN. Ultrasonic welding of advanced thermoplastic composites: an investigation on energy-directing surfaces. Adv Polym Technol Jun. 2010;29(2):112–21. https://doi.org/10.1002/ADV.20178.
[40] Sarantinos N, Kostopoulos V, Di Vita G, Campoli G, Bricout L. Micro-pins: the next step in composite–composite and metal–composite joining. CEAS Sp. J. 2019 113 May 2019;11(3):351–8. https://doi.org/10.1007/S12567-019-00251-1.
[41] Roirand H, Malard B, Hor A, Saintier N. Effect of laser scan pattern in laser powder bed fusion process: the case of 316L stainless steel. Procedia Struct Integr Jan. 2022;38(C):149–58. https://doi.org/10.1016/J.PROSTR.2022.03.016.
[42] ASTM B962-15 Standard Test Methods for Density of Compacted or Sintered Powder Metallurgy (PM) Products Using Archimedes' Principle, American Society for Testing and Materials, Pennsylvania, United States." https://www.astm.org/b0962-15.html (accessed Nov. 30, 2022).

[43] Washko SD, Aggen G. Wrought stainless steels, properties and selection: irons, steels, and high-performance alloys, 1. ASM Handb.; 1990. p. 841–907. https://doi.org/10.31399/ASM.HB.V01.A0001046.
[44] Charmi A, Falkenberg R, Ávila L, Mohr G, Sommer K, Ulbricht A, et al. Mechanical anisotropy of additively manufactured stainless steel 316L: an experimental and numerical study. Mater Sci Eng, A Jan. 2021;799:140154. https://doi.org/10.1016/J.MSEA.2020.140154.
[45] Wang P, Zou B, Ding S, Huang C, Shi Z, Ma Y, et al. Preparation of short CF/GF reinforced PEEK composite filaments and their comprehensive properties evaluation for FDM-3D printing. Composites Part B Oct. 2020;198:108175. https://doi.org/10.1016/J.COMPOSITESB.2020.108175.
[46] Leone FA, Dávila CG, Girolamo D. Progressive damage analysis as a design tool for composite bonded joints. Composites Part B Aug. 2015;77:474–83. https://doi.org/10.1016/J.COMPOSITESB.2015.03.046.
[47] Borges MF, Amancio-Filho ST, Dos Santos JF, Strohaecker TR, Mazzaferro JAE. Development of computational models to predict the mechanical behavior of Friction Riveting joints. Comput Mater Sci Mar. 2012;54(1):7–15. https://doi.org/10.1016/J.COMMATSCI.2011.10.031.
[48] Komatsu S, Takahara A, Kajiyama T. Effect of cyclic fatigue conditions on nonlinear dynamic viscoelasticity and fatigue behaviors for short glass-fiber reinforced nylon 6. Polym. J. 2003 3511 2003;35(11):844–50. https://doi.org/10.1295/polymj.35.844.
[49] Schijve J. Fatigue of structures and materials. second ed. Springer Netherlands; 2009. https://doi.org/10.1007/978-1-4020-6808-9.
[50] Khelif R, Chateauneuf A, Chaoui K. Statistical analysis of HDPE fatigue lifetime. Meccanica Dec. 2008;43(6):567–76. https://doi.org/10.1007/S11012-008-9133-7/METRICS.
[51] Effertz PS, Infante V, Quintino L, Suhuddin U, Hanke S, Dos Santos JF. Fatigue life assessment of friction spot welded 7050-T76 aluminium alloy using Weibull distribution. Int J Fatig Jun. 2016;87:381–90. https://doi.org/10.1016/J.IJFATIGUE.2016.02.030.
[52] Uematsu Y, Tokaji K. Comparison of fatigue behaviour between resistance spot and friction stir spot welded aluminium alloy sheets Jan. 2013;14(1):62–71. https://doi.org/10.1179/136217108X338908. doi: 10.1179/136217108X338908.
[53] Khashaba UA. Fatigue and reliability analysis of unidirectional GFRP composites under rotating bending loads Jul. 2016;37(4):317–31. https://doi.org/10.1177/0021998303037004680. doi: 10.1177/0021998303037004680.
[54] AbdAllah MH, Abdin EM, Selmy AI, Khashaba UA. Effect of mean stress on fatigue behaviour of GFRP pultruded rod composites. Composer Part A Appl Sci Manuf Jan. 1997;28(1):87–91. https://doi.org/10.1016/S1359-835X(96)00090-5.
[55] Sakin R, Ay I. Statistical analysis of bending fatigue life data using Weibull distribution in glass-fiber reinforced polyester composites. Mater Des Jan. 2008;29(6):1170–81. https://doi.org/10.1016/J.MATDES.2007.05.005.
[56] Feistauer EE. Ultrasonic joining of through-the-thickness reinforced metal-composite hybrid structures. Ph.D. Diss. Tech. Univ. Hamburg; 2019. https://doi.org/10.15480/882.1956.
[57] Zhao L, Xin A, Liu F, Zhang J, Hu N. Secondary bending effects in progressively damaged single-lap, single-bolt composite joints. Results Phys Jan. 2016;6:704–11. https://doi.org/10.1016/J.RINP.2016.08.021.
[58] Ekh J, Schön J, Melin LG. Secondary bending in multi fastener, composite-to-aluminium single shear lap joints. Composites Part B Apr. 2005;36(3):195–208. https://doi.org/10.1016/J.COMPOSITESB.2004.09.001.
[59] Barkia B, Aubry P, Haghi-Ashtiani P, Auger T, Gosmain L, Schuster F, et al. On the origin of the high tensile strength and ductility of additively manufactured 316L stainless steel: multiscale investigation. J Mater Sci Technol Mar. 2020;41:209–18. https://doi.org/10.1016/J.JMST.2019.09.017.
[60] Sikder P, Challa BT, Gummadi SK. A comprehensive analysis on the processing-structure-property relationships of FDM-based 3-D printed polyetheretherketone (PEEK) structures. Materialia May 2022;22:101427. https://doi.org/10.1016/J.MTLA.2022.101427.
[61] André NM, Goushegir SM, Dos Santos JF, Canto LB, Amancio-Filho ST. Friction Spot Joining of aluminum alloy 2024-T3 and carbon-fiber-reinforced poly(phenylene sulfide) laminate with additional PPS film interlayer: microstructure, mechanical strength and failure mechanisms. Composites Part B Jun. 2016;94:197–208. https://doi.org/10.1016/J.COMPOSITESB.2016.03.011.
[62] Jung KW, Kawahito Y, Takahashi M, Katayama S. Laser direct joining of carbon fiber reinforced plastic to zinc-coated steel. Mater Des May 2013;47:179–88. https://doi.org/10.1016/J.MATDES.2012.12.015.
[63] Goushegir SM, Dos Santos JF, Amancio-Filho ST. Fatigue performance of metal–composite friction spot joints. Materials Aug. 2021;14(16):4516. https://doi.org/10.3390/MA14164516. 2021, Vol. 14, *Page* 4516.
[64] Andrzejewska A, Pejkowski L, Topoliński T. Tensile and fatigue behavior of additive manufactured polylactide. October 2019;6(5):272–80. https://doi.org/10.1089/3DP.2017.0154.
[65] Pop MA, Zaharia SM, Chicos LA, Lancea C, Stamate VM, Buican GR, et al. Effect of the infill patterns on the mechanical properties of the carbon fiber 3D printed parts. IOP Conf Ser Mater Sci Eng Mar. 2022;1235(1):012006. https://doi.org/10.1088/1757-899X/1235/1/012006.
[66] Zaharia SM, Enescu LA, Pop MA. Mechanical performances of lightweight sandwich structures produced by material extrusion-based additive manufacturing. Polym Aug. 2020;12(8):1740. https://doi.org/10.3390/POLYM12081740. 2020, Vol. 12, Page 1740.
[67] Bernardi M, Suhuddin UFH, Fu B, Gerber JP, Bianchi M, Ostrovsky I, et al. Fatigue behaviour of multi-spot joints of 2024-T3 aluminium sheets obtained by refill Friction Stir Spot Welding with polysulfide sealant. Int J Fatig Jan. 2023:107539. https://doi.org/10.1016/J.IJFATIGUE.2023.107539.
[68] Schijve J. Fatigue of structures and materials. Fatigue Struct. Mater. 2009:1–622. https://doi.org/10.1007/978-1-4020-6808-9/COVER.
[69] Schmidt H-J, Schmidt-Brandecker B. Fatigue & Damage Tolerance 2017.
[70] Belei C, Pommer R, Amancio-Filho ST. Optimization of additive manufacturing for the production of short carbon fiber-reinforced polyamide/Ti-6Al-4V hybrid parts. Mater Des Jul. 2022;219:110776. https://doi.org/10.1016/J.MATDES.2022.110776.
[71] Zhang W, Zhou Z, Scarpa F, Zhao S. A fatigue damage meso-model for fiber-reinforced composites with stress ratio effect. Mater Des Oct. 2016;107:212–20. https://doi.org/10.1016/J.MATDES.2016.06.040.